



# Role of particle crushing on particle kinematics and shear banding in granular materials

Gang Ma<sup>1,2</sup> · Richard A. Regueiro<sup>2</sup> · Wei Zhou<sup>1</sup> · Qiao Wang<sup>1</sup> · Jiaying Liu<sup>1</sup>

Received: 10 May 2017 / Accepted: 18 December 2017 / Published online: 8 January 2018  
© Springer-Verlag GmbH Germany, part of Springer Nature 2018

## Abstract

The paper provides an in-depth exploration of the role of particle crushing on particle kinematics and shear banding in sheared granular materials. As a two-dimensional approximation, a crushable granular material may be represented by an assembly of irregularly shaped polygons to include shape diversity of realistic granular materials. Particle assemblies are subjected to biaxial shearing under flexible boundary conditions. With increasing percentage of crushed particles, mesoscale deformation becomes increasingly unstable. Fragmented deformation patterns within the granular assemblies are unable to form stable and distinct shear bands. This is confirmed by the sparsity of large fluctuating velocities in highly crushable assemblies. Without generating distinct shear bands, deformation patterns and failure modes of a highly crushable assembly are similar to those of loose particle assemblies, which are regarded as diffuse deformation. High degrees of spatial association amongst the kinematical quantities confirm the key role that non-affine deformation and particle rotation play in the generation of shear bands. Therefore, particle kinematical quantities can be used to predict the onset and subsequent development of shear zones, which are generally marked by increased particle kinematic activity, such as intense particle rotation and high granular temperature. Our results indicate that shear band thickness increases, and its speed of development slows down, with increasing percentage of crushed particles. As particles crush, spatial force correlation becomes weaker, indicating a more diffuse nature of force transmission across particle contacts.

**Keywords** Force transmission · Granular materials · Granular temperature · Particle crushing · Particle kinematics · Shear banding

## 1 Introduction

Understanding the connection between strain localization and individual particle kinematics in granular materials is a fundamental challenge in geomechanics research. In the case of earth slope failures that have accumulated sizable slip throughout their active history, it is apparent that shear deformation localizes dynamically into very thin zones. Unraveling how slip localizes in such thin zones, how the

thicknesses of shear bands evolve as a function of different loading conditions, and what the implications for stability of sliding are, may hold the key for understanding a number of outstanding problems in geotechnics, such as origins of earth slope failure.

Although shear banding in granular materials has been long observed through experimental study, its particle-scale underpinnings, interdependencies, and variabilities under different loading conditions, and initial state and loading history, have not been fully explored. The difficulty lies in how to extract particle-scale information for analysis. Recent developments in particle-scale spatial-resolution laboratory experiments allow considerably more accurate observation of granular material mechanics at the particle length scale. Measurement of contact forces and particle kinematics in two-dimensional idealized assemblies of photoelastic disks has been obtained and analyzed [38, 57]. X-ray computed tomography (CT) image

---

✉ Gang Ma  
magang630@whu.edu.cn

<sup>1</sup> State Key Laboratory of Water Resources and Hydropower Engineering Science, Wuhan University, Wuhan 430072, China

<sup>2</sup> Department of Civil, Environmental, and Architectural Engineering, University of Colorado Boulder, Boulder, CO 80309-0428, USA

acquisition and processing has also greatly advanced the quantification of particle morphology, orientation, and contact configuration of granular materials [11]. More recently, by combining 3D X-ray diffraction, X-ray tomography, and a numerical force interference technique, it is possible to quantify interparticle forces and their heterogeneity in an assembly of quartz particles undergoing one-dimensional compression [20]. Developments in experimental techniques have stimulated advances in measurement and representation of granular material microstructure at smaller and smaller spatial length scales [3, 4, 6, 10, 17–19, 43, 46, 51, 58]. These techniques derive measurements of the trajectory of each particle and interparticle contact forces and have in turn enabled precise quantification of shear band patterning, inclination, and thickness. More importantly, these techniques enable precise detection of individual particle morphology and kinematics, providing detailed particle position and contact maps, and calculations of local void ratios [53]. The X-ray CT can also be used in the quantification of particle breakage and the resulting particle size distribution and shape evolution [2, 23].

Another contribution toward revealing particle-length-scale information of granular materials comes from discrete element-type numerical simulations, such as the discrete element method (DEM). Since its first introduction, DEM has been used extensively in reproducing macroscopic mechanical response and investigating the particle-scale behavior of granular materials. There is no doubt of DEM's prevalence in particle-scale analysis of shear banding or strain localization in granular materials. The initiation and development of shear bands under different controlling parameters, e.g., particle rolling resistance [21, 22, 40], particle shape [37, 64], initial packing state [12, 13, 36, 67], and boundary conditions [9], are the main scope of these DEM studies. The simulation results are statistically analyzed with respect to particle kinematics (translation and rotation) [21, 22, 37, 40, 64], column-like structure [21, 22, 40], fabric anisotropy [12, 36], void distribution [13, 67], and so on. By adopting numerical particle-based methods, such as DEM, while including laboratory experiments with particle-scale measurements, researchers have an opportunity to integrate such information on kinematics at the particle scale to probe simultaneously the macro-(continuum-scale) and micro-(particle-scale) mechanical behavior of granular materials [56].

However, although almost all of the aforementioned studies highlighted the importance of particle kinematics in the formation of shear bands, few have focused on the additional influence of particle crushing. It is generally accepted and recently demonstrated by Ma et al. [33, 66] that the formation of shear bands in granular materials is

influenced by particle crushing. Particles within shear bands are prone to crushing through surface erosion, chipping, and fragmentation when exposed to substantial shear stresses. Within the framework of combined finite and discrete element modeling (FDEM) of granular materials, this paper aims to investigate the role of particle crushing and kinematics on the onset and subsequent development of strain localization in granular materials. Fundamental aspects of combined FDEM can be found in Munjiza et al. [41]. Recent developments in particle shape representation and cohesive crack modeling make the combined FDEM an ideal tool for modeling irregularly shaped and crushable granular materials [29–32, 34, 35, 65]. Following a brief description of combined FDEM and the particle crushing model, simulation results of 2D plane strain biaxial tests of particle assemblies with different levels of “crushability” (percentage of particles that have crushed) are presented. Microstructures and their evolution during shearing are carefully examined and analyzed. Suggestions for extending these results to continuum constitutive modeling are then provided.

## 2 Combined FDEM modeling of biaxial tests

### 2.1 Principles of combined FDEM

A typical combined FDEM simulation contains a large number of interacting particles, each of which is discretized into a finite element mesh. As the simulation proceeds, these bodies can deform, translate, rotate, interact, and fracture or fragment when satisfying certain failure criteria and thus produce new particles also represented by finite element meshes. The newly generated particles can then undergo further motion, interaction, deformation, and fracturing. A contact detection algorithm is employed to first detect all particle pairs that are in contact and eliminate those that are far apart and cannot possibly be in contact. Subsequently, a contact interaction algorithm is used to calculate interaction forces between all particle pairs. The contact interaction algorithm takes advantage of the finite element discretization of the discrete particles. In the normal direction, repulsive forces are applied to enforce impenetrability, while in the tangential direction, frictional forces are applied. An explicit central difference in time integration scheme is employed to solve the equations of motion for the discretized system and update the nodal coordinates every time step.

In combined FDEM, particle crushing is explicitly modeled using the cohesive crack model. Cohesive interface elements (CIEs) with zero thickness are inserted between the edges of all adjacent bulk finite element pairs

at the beginning of the simulation. For brevity, only key details of the particle crushing model will be repeated, whereas for full details of the model, as well as a critical discussion on the choice of model parameters, the reader is referred to prior publications [31, 32]. It should be noted that a remeshing technique can be implemented in the combined FDEM, but the computational cost will be extremely high when simulating crushable granular materials. As remeshing is not performed, and mesh topology is never updated during the simulation, the particles will not continue to become smaller during the loading process (i.e., no less than about one fifth of its parent particle size).

The CIE can yield and break due to excessive tension, shearing, or their combinations subject to mix-mode loading. Thus, the CIE is assumed to fail if the following coupled criterion involving tensile strength and shear strength is satisfied:

$$\left\langle \frac{t_n}{f_t} \right\rangle^2 + \left\langle \frac{t_{\text{shear}}}{f_s} \right\rangle^2 \geq 1 \quad (1)$$

where  $\langle \cdot \rangle$  is the Macaulay bracket considering that compressive (negative) normal traction does not affect the onset of damage. Note that here tensile stress is positive and compressive stress is negative. The tensile strength,  $f_t$ , is assumed to be constant, while  $f_s$  is defined by the Mohr–Coulomb criterion with a tension cutoff  $f_s = c - t_n \tan \varphi_i$ , where  $c$  is the internal cohesion,  $\varphi_i$  is the material internal friction angle, and  $t_n$  is the normal stress perpendicular to the shear direction.

The proposed criterion correctly captures the onset of damage under pure tension (i.e.,  $t_n = f_t$ ) and pure shearing (i.e.,  $t_{\text{shear}} = f_s$ ), as well as provides a simple interpolation of the mix-mode damage threshold for the combined cases (i.e.,  $0 < t_n < f_t$ ,  $0 < t_{\text{shear}} < f_s$ ). When a CIE is completely damaged, the CIE is removed from the model, and a physical discontinuity is formed; therefore, the model locally transforms from a continuum to a discontinuum. The newly created discontinuity is automatically recognized and modeled by the contact interaction algorithm.

## 2.2 Biaxial test simulation

Simulated biaxial tests are performed on a polydisperse assembly of polygonal particles with narrow particle size distribution (PSD). Particles are generated by means of Voronoi tessellation to include the shape diversity of a realistic granular material. The shape characteristics, such as elongation and circularity, are statistically close to the priori knowledge about the particle shapes. The equivalent particle diameter,  $d^*$ , which is defined as the diameter of a circle with an equivalent area to an irregularly shaped particle, falls within the 10 mm to 40 mm range, and the

mean particle diameter  $d_{50}^*$  is 25 mm. The assembly consists of 10,217 particles, and the PSD shown in Fig. 1a has a similar shape as that of Toyoura sand. The use of a narrow PSD in the simulation allows the effects of particle breakage to be easily observed. Note that the interparticle friction coefficient is temporarily set to zero during sample preparation to obtain a relatively dense packing, and particle crushing is also disabled. The final configuration of the numerical specimen shown in Fig. 1b has a void ratio of 0.156. Such small void ratio is selected to facilitate the onset and development of localized failure mode.

The virtual biaxial compression test setup is depicted in Fig. 1b, in which the particle assembly is confined with a pair of smooth rigid walls on top and bottom and two flexible membranes left and right. The membrane elements can only support in-plane forces and have no bending stiffness, are allowed to deform flexibly to mimic the laboratory specimen deformation, and are capable of better replicating the uniformly applied confining pressure during the shearing process. The particle assembly is initially compressed isotropically until the prescribed confining pressure is reached. Then, the assembly is sheared by displacing the top and bottom walls toward each other at a constant velocity, while keeping confining pressure constant. Gravity is not considered. To ensure the assembly is sheared under quasi-static condition, the strain rate is set to 0.02/s and the corresponding inertial number  $I \approx 10^{-5}$  is less than the limiting inertial number  $10^{-3}$  [1].

Similar to a DEM simulation, the contact interaction model in the combined FDEM determines the mechanical behavior between two contacting particles. The repulsive and frictional forces between contacting elements are calculated using a distributed contact force penalty function method. Two penalty terms are required as input parameters, i.e.,  $p_n$  and  $p_t$ , where the subscripts represent the normal and tangential directions, respectively. It is noted that as the penalty parameters tend to infinity, an impenetrability condition and complete friction mobilization are approached. However, in practice, finite values for the penalty parameter must be adopted, as large values of  $p_n$  and  $p_t$  lead to temporal integration problems. Although the overall response of a model will be artificially reduced as a result of permitting some amount of element interpenetration and interelement sliding, the relative contribution to the overall model stiffness can be made negligible if sufficiently large, yet practical values of  $p_n$  and  $p_t$  are adopted. As suggested by Tatone and Grasselli [55], the assumption of normal penalty parameter equal to the tangential penalty parameter can produce the correct elastic response of rocks.

The “crushability” of a particle is characterized by the embedded CIE’s strength and quantified by three parameters: uniaxial tensile strength,  $f_t$ , internal friction angle,  $\varphi_i$ ,

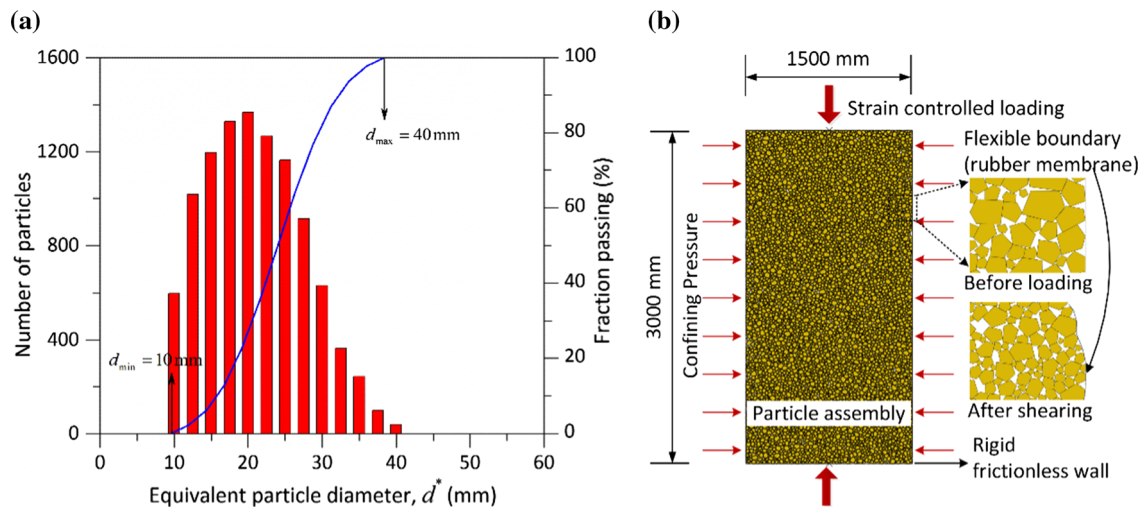


**Fig. 1** **a** Particle size distribution (PSD) and **b** setup of biaxial numerical simulation

and cohesive strength,  $c$ . For simplicity, the internal friction angle,  $\varphi_i$ , and the ratio of the unconfined compressive strength (UCS)  $f_c$  to the tensile strength,  $f_c/f_t$ , are set to  $40^\circ$  and  $12^\circ$ , respectively. Therefore, one can use the UCS to calculate the other two strength parameters  $f_t = f_c/12$  and  $c = f_c(1 - \sin \varphi_i)/(2 \cos \varphi_i)$ . This is particularly convenient in the description of particle crushability and subsequent analysis of simulation results. The contact interparticle friction coefficient is equal to 0.6, which yields similar values of macro-mechanical friction angles to those obtained in real granular materials, such as gravel or sand. Four levels of particle crushability are considered using CIEs:  $f_c = 30, 60, 90,$  and  $120$  MPa, respectively. Generally, a particle assembly with a higher degree of crushability ( $f_c = 30$  MPa) means that its particles are more vulnerable to crush. Other parameters are selected for general applications rather than for a specific granular material. The input parameters are summarized in Table 1.

### 2.3 Macroscopic response

For convenience, each simulation is labeled by boundary condition types, initial confining pressure, and level of particle crushability. The abbreviation FM denotes flexible membrane (FM) boundary condition. Particle crushability is denoted by the unconfined compressive strength (UCS)  $f_c$ . For example, FM-2.0-120 indicates a biaxial compression test with flexible boundary condition under an initial confining pressure of 2.0 MPa and UCS  $f_c = 120$  MPa. To obtain the “real” stress tensor inside the assembly, a mask is defined in Fig. 2a. Due to distortion of the assembly with flexible boundaries, the particles that bulge outside are not included in the mask for calculating stress, and the mask is changed at each 0.1% axial strain. As each particle, no matter it is an intact one or a newly generated one due to

**Table 1** Simulation parameters used in numerical biaxial tests

Parameter	Value	Units
Solid elements		
Mass density, $\rho$	2700	kg/m <sup>3</sup>
Young's modulus, $E$	40	GPa
Poisson's ratio, $\nu$	0.2	–
Cohesive elements		
Tensile strength, $f_t$	2.5, 5.0, 7.5, 10	MPa
Friction angle of intact material, $\varphi_i$	$40^\circ$	$^\circ$
Friction angle of fractures, $\varphi_f$	$30^\circ$	$^\circ$
Cohesion, $c$	6.99, 13.99, 20.98, 23.98	MPa
Mode I fracture energy, $G_I$	100	N/m
Mode II fracture energy, $G_{II}$	500	N/m
Contact law		
Interparticle sliding friction, $\mu$	0.6	–
Normal penalty, $p_n$	$4.0 \times 10^{11}$	N/m <sup>3</sup>
Tangential penalty, $p_t$	$4.0 \times 10^{11}$	N/m <sup>3</sup>

the breakage of parent particle, is associated with a finite element mesh. The average stress tensor inside the mask is calculated as [48]:

$$\sigma_{ij} = \frac{1}{A} \sum_{p=1}^{N_p} \sigma_{ij}^p A^p \quad (2)$$

where the summation is over  $N_p$  solid elements inside the mask with area  $A$ ,  $\sigma_{ij}^p$  is the stress tensor of the  $p$ th solid element, and  $A^p$  is the area of the  $p$ th solid element.

Components of the assembly stress tensor  $\sigma_{ij}$  can also be calculated by dividing the resultant force applied on the rigid wall by the relevant assembly size to obtain the major



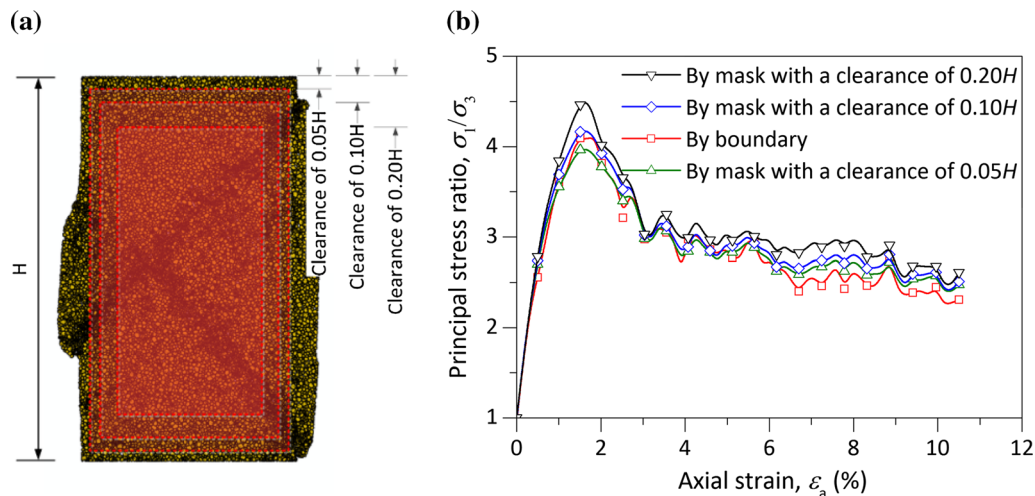


**Fig. 2** **a** Definition of mask used in calculation of assembly stress tensor; **b** assembly stress tensor calculated by boundary and three masks with different clearance

principal stress (now assuming positive in compression)  $\sigma_1$ , while the minor principal stress  $\sigma_3$  is directly applied on the surfaces with flexible membranes. The principal stress ratio calculated using the mask and directly from the boundaries is compared in Fig. 2b. It can be seen that the average stress tensor inside each mask is roughly coincident with the stress values calculated at the boundaries. As deformation continues, curves begin to slightly diverge from each other, and noticeable differences are observed in the peak values. As the peak stress inside the mask with a clearance of  $0.1H$  is closest to the value calculated at the boundary, this mask is used in subsequent particle assembly stress tensor calculations.

Principal stress ratio  $\sigma_1/\sigma_3$  and volumetric strain  $\epsilon_v$  (using mask with clearance  $0.1H$ ) are plotted versus axial strain in Fig. 3a, b. The simulation results, including strain softening and shear dilatancy, are typical of stress and strain response for drained biaxial tests in plane strain conditions [5]. With lower percentage of particle crushing, i.e., higher CIE strength,  $\sigma_1/\sigma_3$  versus  $\epsilon_a$  plots exhibit a steeper slope (higher initial stiffness), notable post-peak strain softening, and strong dilation. As additional shear force is required to dilate the particle assemblies, a dilative assembly generally mobilizes greater shear strength than a contractive assembly. Once peak strength has been overcome through continued shearing, the resistance to applied shear stress reduces, and strain softening is observed. FM-2.0-120 shows the largest stress drop after peak, accompanied by the strongest bulk dilatancy. With increasing particle crushability (i.e., lower CIE strength), strain softening becomes more mild and in fact vanishes in FM-2.0-30. Four strain levels labeled in Fig. 3a will be used in subsequent sections to illustrate progressive formation of strain localization. The volumetric response becomes

progressively more compressive with increase in particle crushing. This behavior is clearly a result of extensive particle crushing, which suppresses the mobilization of particle assembly dilation. The stress–strain curves of less crushable assemblies are associated with significant stress drops and local fluctuations, especially in the post-peak strain softening regime. After an axial strain of  $\approx 8\%$ , the stress ratio reaches a steady-state value with small oscillations. The principal stress ratios of four assemblies reach the same steady-state value of  $\approx 2.8$ . However, the rate of change of volumetric strain at 8–11% axial strain is small but still perceptible.

Particle size distributions (PSDs) of four simulations at the axial strain of 10% are shown in Fig. 3c, in which the percentage by mass finer is plotted against particle size (i.e., equivalent particle diameter) on semilogarithmic axis. It is clear that substantial particle breakage takes place, which changes the overall trend of PSDs as compared to their initial distribution. As particle crushability increases, the grading curves gradually shift to left and change from concave downward to convex upward, while particles of the largest size remain throughout. The convex-type PSD is attributed to the fact that particles in FDEM simulation cannot keep breaking into smaller particles. Therefore, the smallest particle size will not continuously decrease. As explained in Sect. 2.1, we need to add a remeshing algorithm into the FDEM to generate an increasing range of particle sizes. This function is not yet implemented in the present FDEM studies, mainly due to it becoming too much computationally expensive. Figure 3d shows the particle size distributions displayed in terms of the frequency counts with a bin size of 2.5 mm. As can be seen, starting at the largest particles (40 mm), the lower bins increase in

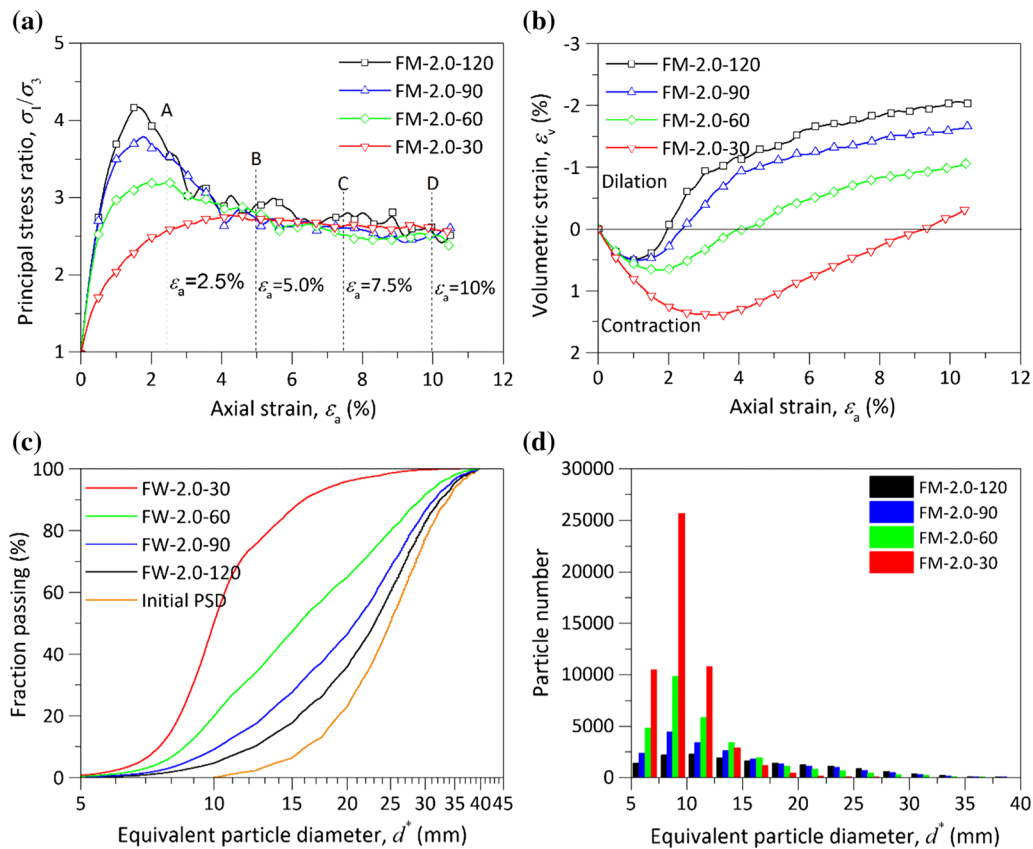


**Fig. 3** Macroscopic responses obtained for assemblies with different crushability: **a** principal stress ratio; **b** volumetric strain; **c** particle size distributions at the axial strain of 10%; **d** number of particles plotted as functions of particle size at the axial strain of 10%

quantity, reaching a peak, after which the subsequent bins display a rapidly decreasing quantity.

### 3 Characteristics of particle kinematics

#### 3.1 Distribution of kinematical quantities

Different spatially distributed quantities are used to demonstrate strain localization in a particle assembly, such as void ratio, particle rotation, local shear intensity, local shear strain, energy dissipation, relative displacement, and “granular temperature.” In this section, particle rotation from the beginning of shearing is used to identify localization of strain into shear zones. The rotation of a particle/fragment is calculated by averaging the rotation of each solid element that belongs to this particle/fragment. The deformation of a solid element, i.e., finite element used in the mesh discretization of a particle, is ignorable when compared with its translation and rotation. Therefore, the rotation of a solid element belonging to that fragment can be easily determined by coordinate transformation. Shear zones are generally marked by significant particle rotation, so it can be taken as a well-recognized identifier of strain

localization within granular materials [21, 25]. Figures 4 and 5 show the deformed specimen geometries and contours of particle rotation at different axial strain levels for FM-2.0-120 (low crushability) and FM-2.0-30 (high crushability), respectively. As a consequence of flexible membranes bounding the specimen laterally, bulging is observed in all of the subplots. At each stage of loading, rotation and deformation are concentrated within small regions, which demonstrates that the motions of individual particles are not random and unrelated, but instead interact with the motions of nearby particles to form large long-range deformation structures. It is clear that the shear band pattern is sensitive to particle crushability.

As shown in Fig. 4, the highly rotated particles concentrate in an x-shaped zone transversing the low crushable assembly (FM-2.0-120), which manifests as two conjugate shear bands with developed and distinct configuration. As shearing continues, the deformation is concentrated within much thicker shear bands. When shearing to large strains, shear bands become stationary and persistent. The lateral membranes are seen to deform severely to form local “wraps” around the ends of the shear bands, which is a clear indication of strong dilation associated with strain localization. Back to Fig. 4a, although the assembly has

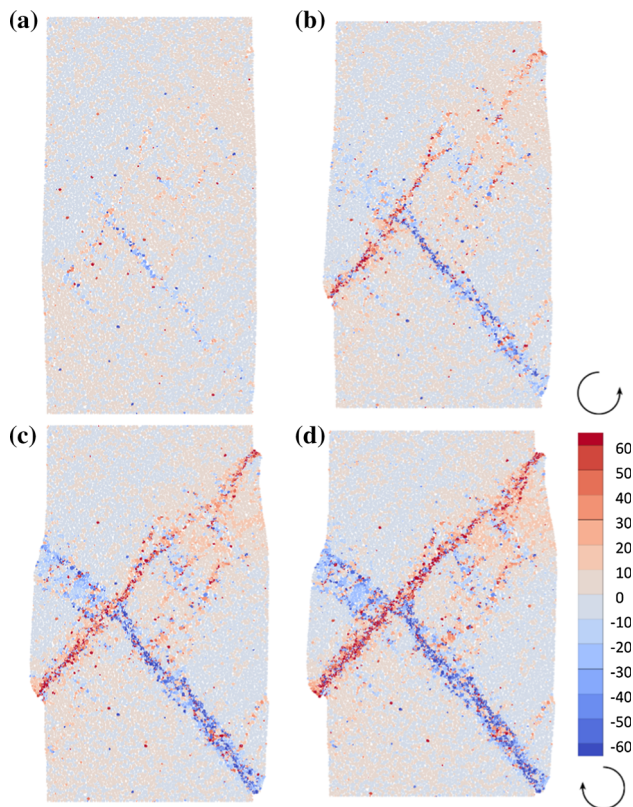


**Fig. 4** Contours of particle rotation (in degrees) at different axial strain levels for FM-2.0-120: **a**  $\varepsilon_a = 2.5\%$ ; **b**  $\varepsilon_a = 5.0\%$ ; **c**  $\varepsilon_a = 7.5\%$ ; **d**  $\varepsilon_a = 10\%$

entered a strain softening stage (see Fig. 3a), the shear bands are still in development. With an increase in particle crushability, rather than two dominant X-shaped shear bands developing, one or two major shear bands are observed and accompanied by less-developed shear bands intersecting with the major bands (see Fig. 5 for FM-2.0-30). For the highly crushable assembly (FM-2.0-30), the distribution and failure patterns are significantly different from the low crushability FM-2.0-120, where clear and persistent shear bands can be identified. Even though many irregularly and locally banded domains exist, the distribution of these domains is blurry and disorganized (see Fig. 5), and they fail to form a connected zone.

In a dense assembly, contacts of individual particles give rise to local fluctuating components of stress, strain rate, and local void ratio with reference to the macroscopic deformation. The ensemble average of these fluctuating components allows the time-averaged, mean-field values of stress, strain rate, and void ratio parameters to be established. A pseudo-“granular temperature” is calculated from these local fluctuating values to quantify a granular state in a form similar to the definition of thermodynamic temperature of fluids [8]. Campbell [8] pointed out that granular temperature is generated by either a collisional

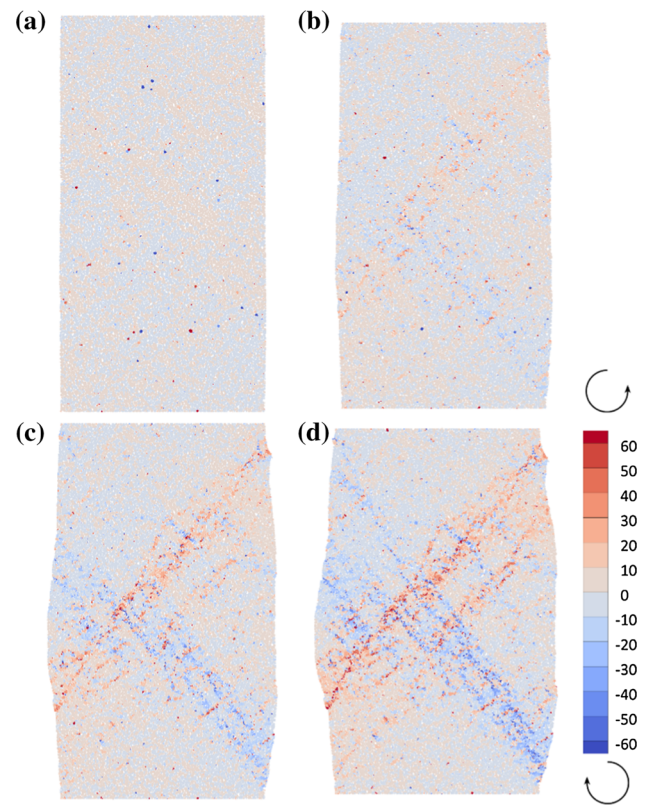


**Fig. 5** Contours of particle rotation (in degrees) at different axial strain levels for FM-2.0-30: **a**  $\varepsilon_a = 2.5\%$ ; **b**  $\varepsilon_a = 5.0\%$ ; **c**  $\varepsilon_a = 7.5\%$ ; **d**  $\varepsilon_a = 10\%$

mechanism or a streaming mechanism. Because of the polygonal particle shapes, interparticle contacts will randomize the impact velocity, thus converting the mean motion of the flow into granular temperature. This mechanism is an exact analog of the thermal motion of molecules. Following statistical thermodynamics of molecular fluids, the granular temperature  $T$  of particle  $i$  is calculated using the fluctuating velocity  $\mathbf{v}_i^{\text{rel}}$  as follows:

$$T_i = \left( \frac{v_{i,x}^{\text{rel}}}{v^*} \right)^2 + \left( \frac{v_{i,y}^{\text{rel}}}{v^*} \right)^2 \quad (3)$$

where the fluctuating velocity of a particle  $\mathbf{v}_i^{\text{rel}}$  is defined as the vector difference between the particle velocity  $\mathbf{v}_i$  and a mean local velocity  $\bar{\mathbf{v}}_i$  [24, 50]. The mean local velocity is calculated by averaging the particle velocities surrounding the selected particle within a certain preset region. The reference velocity  $v^* = \sqrt{0.1d_{50}g}$  is calculated to non-dimensionalize the granular temperature, where  $g$  is the gravitational acceleration and  $d_{50}$  is the mean diameter of the particles in the initial particle assembly. The space-averaged granular temperature in a two-dimensional system is computed as  $\bar{T} = \frac{1}{2N} \sum_{i=1}^N T_i$  over the region, where  $N$  is the number of particles. It should be noted that



granular temperature can be “absolute zero” for a granular assembly at rest, or a ordered particle assembly in a smooth, static deformation pattern with no fluctuating velocity component, such that  $v_i^{\text{rel}} = 0$ .

As a result of the irregularities of microstructure at the particle scale (i.e., the structural environment around each particle is unique), the particle velocities have a non-affine fluctuating component of zero mean with respect to the mean local velocity. Three snapshots of fluctuating velocity field for FM-2.0-120 are presented in Fig. 6. We can see that large-scale well-organized displacements coexist with a strongly inhomogeneous distribution of amplitudes and directions on different scales. During strain hardening, and prior to shear banding, the assemblies deform in an essentially affine or uniform manner. The deformation is characterized by a presence of separately distributed microbands, which undergo slip deformation due to large relative tangential movement of particles, and organize

themselves into thin obliquely trending bands [24, 56]. It can be seen that the fluctuating velocity vectors form many, randomly distributed circulation cells, also referred to as *vortex structures* at small strain levels (as shown in Fig. 6b) [24, 62]. The vortex or circulation cell has been proven to be a significant transient-correlated particle structure in densely packed granular assemblies [50, 59]. They play an important role in the formation of shear bands. Because particles in between and around vortices have large relative rotations, these structures are located within and around shear bands. As shearing proceeds, the fluctuating velocity vectors rearrange, and the enlarged vortex structures gradually align in opposite directions along a district shear zone. With the increase in particle crushability, the vortex structures become weak, they break down after a short time, and new vortex structures appear. It can be seen in Fig. 7 that such mesoscale structures undergo a transition from ordered to disordered distribution

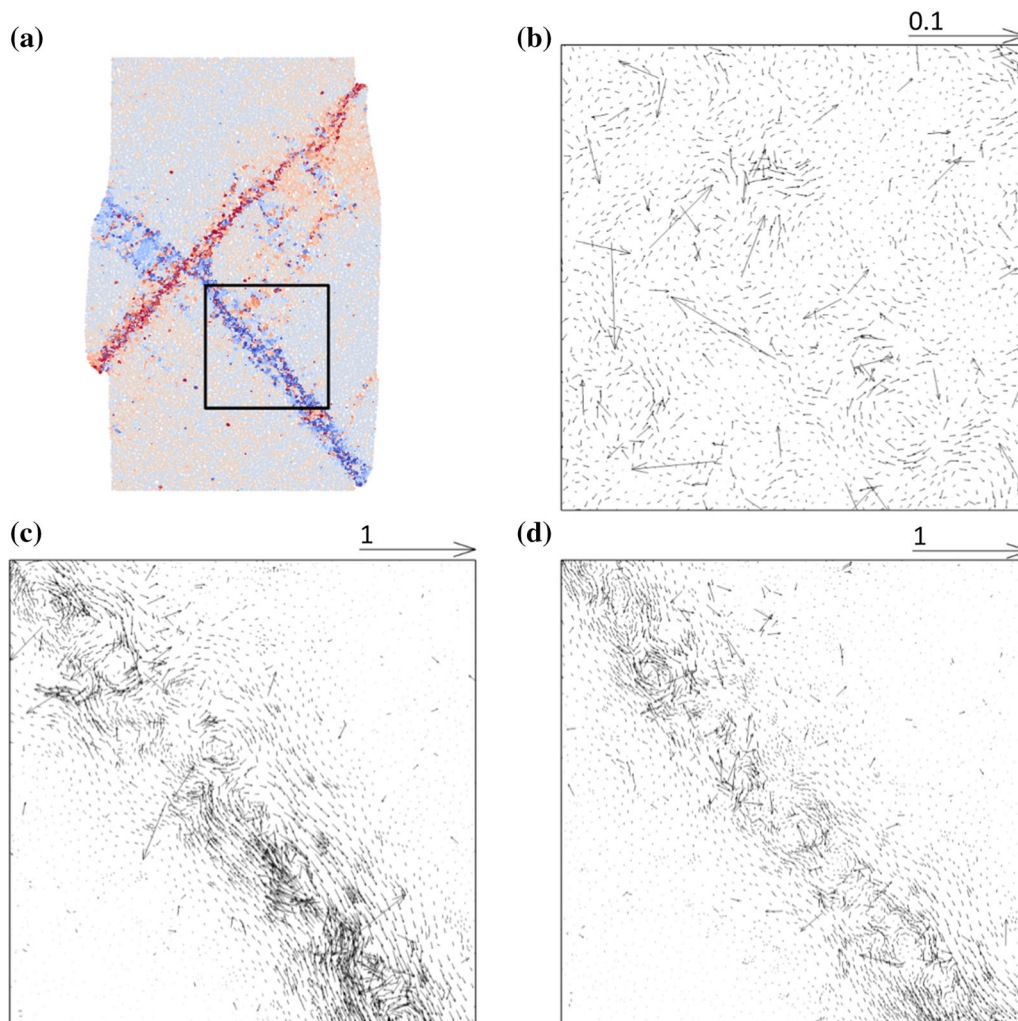


**Fig. 6** Fluctuating velocity vectors within outlined box region in **a** at different axial strains for FM-2.0-120 MPa: **a** observation region; **b**  $\varepsilon_a = 0.8\%$ ; **c**  $\varepsilon_a = 5.0\%$ ; **d**  $\varepsilon_a = 10.0\%$



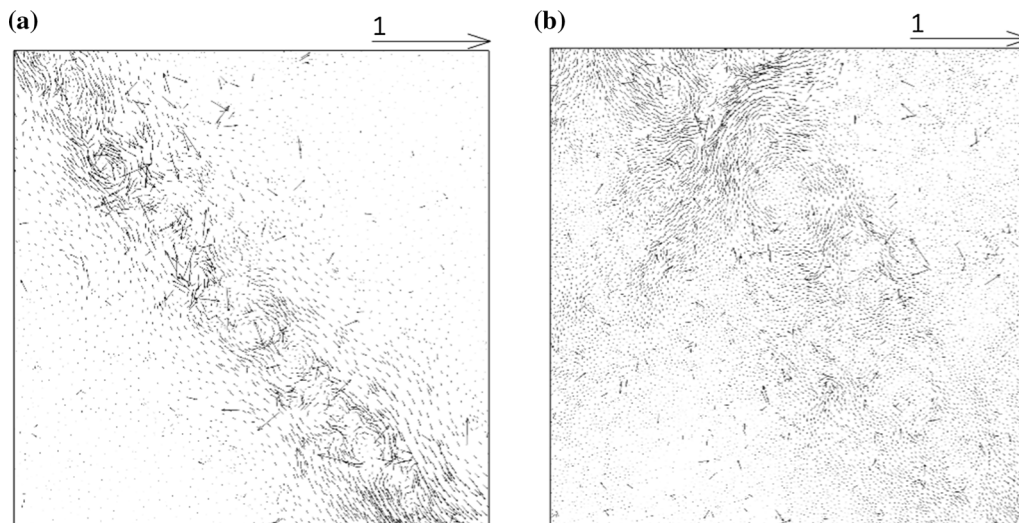


**Fig. 7** Fluctuating velocity vectors at the end of shearing for different crushable assemblies: **a** FM-2.0-120; **b** FM-2.0-30

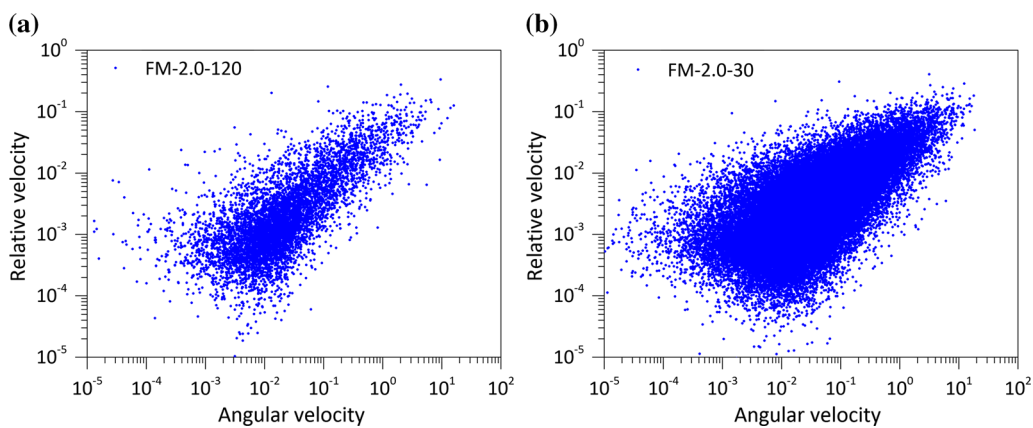


**Fig. 8** Correlation between particle angular velocity and relative velocity: **a** FM-2.0-120; **b** FM-2.0-30

for a highly crushable assembly, which is a sign of loss of correlation with previous particle configurations. As shown in Fig. 8, strong positive linear correlations are observed in both subplots with log–log scales, which implies that highly rotated particles are generally accompanied by intense fluctuation. High degrees of spatial association between particle angular velocity and relative velocity confirm the key role that non-affine deformation and particle rotation play in the onset of shear banding.

We further consider the probability distribution function (pdf) of the  $x$  component of fluctuating velocity as a function of particle crushability. They are typically leptokurtic distributions where the points along the  $x$ -axis are clustered, resulting in a higher peak and fatter tails than the curvature found in a normal distribution (Fig. 9a). At the axial strain of 2.5%, the pdf of lower crushability particle assembly is characterized by broader and stretched tails, which is a sign of developed velocity differences. The

sparsity of large fluctuating velocities in highly crushable assemblies also indicates the fragmented deformation pattern due to intense particle crushing. It is interesting to note that the disparity of pdfs demonstrated in Fig. 9a reduces gradually when assemblies are sheared to large strains (Fig. 9(b)). In order to quantify the tailedness of the probabilistic distribution of fluctuating velocity, we calculate the kurtosis  $g_2 = \mu_4/\sigma^4 - 3$ , where  $\sigma$  is the standard deviation and  $\mu_4$  is the fourth central moment. The kurtosis as a function of axial strain for different crushable assemblies is plotted in Fig. 10a. A larger positive kurtosis value indicates a leptokurtic distribution with fatter tails and higher peak. It is clear in Fig. 10b that kurtosis values during the last 2% of axial strain (9–11%) are close for different levels of crushability. Similar behavior has been found for the  $y$  component of fluctuating velocity (results not shown). In addition to particle fluctuating velocity, both the particle angular velocity and granular temperature of

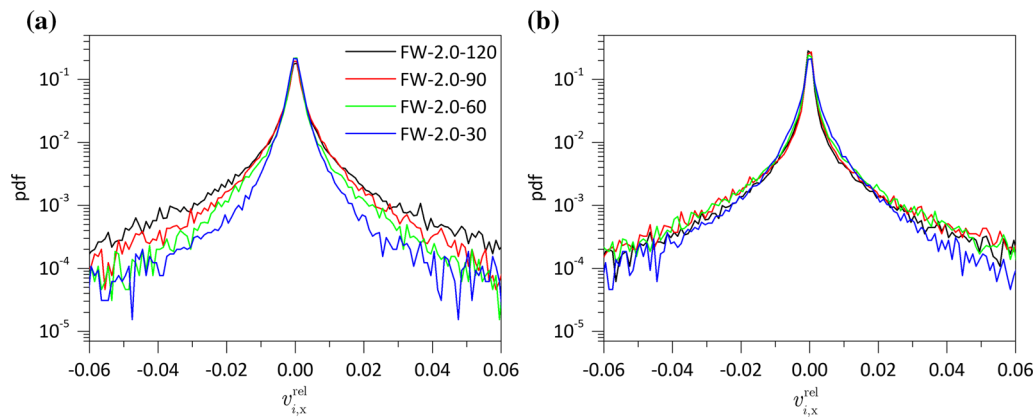


**Fig. 9** Probability distribution function (pdf) of fluctuating velocity at two stages of shearing: **a**  $\varepsilon_a = 2.5\%$ ; **b**  $\varepsilon_a = 10.0\%$

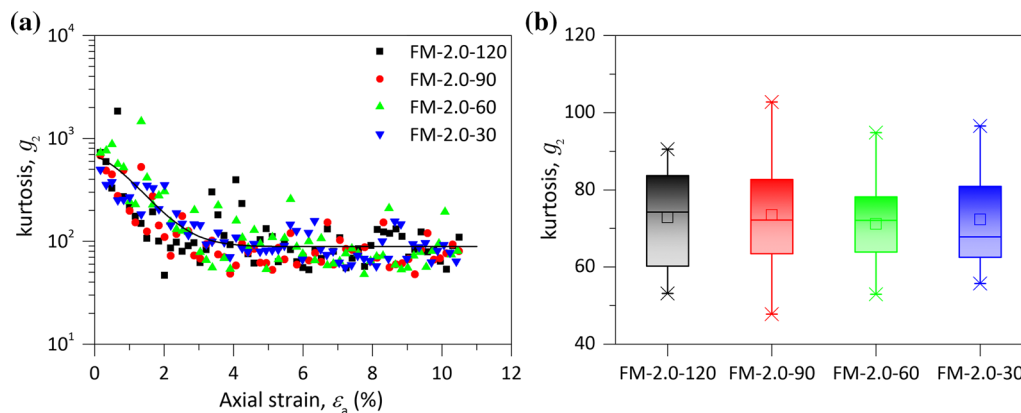


**Fig. 10** **a** Evolutions of kurtosis as a function of axial strain (the solid black line represents the trend line of scattered points); **b** box charts of the kurtosis values during the last 2% of axial strain

assemblies with different levels of crushability have similar distributions when shearing to large enough strains, as will now be demonstrated.

In the case of quasi-static shearing, granular temperature is generated by a complex pattern of particle motions. By decomposing the particle velocity into a mean local velocity and a superimposed fluctuating velocity, we can calculate the granular temperature according to Eq. (4). Figures 11 and 12 plot the contours of granular temperature at different strain levels for FM-2.0-120 and FM-2.0-30, respectively. For ease of visualization, the contour legend uses a logarithmic scale. “High-temperature” particles are concentrated within banded regions, which are wide enough to form macroscopic bands in FM-2.0-120, compared with narrow and isolated regions in FM-2.0-30. Figure 13 plots the evolution of space-averaged temperature inside and outside the shear bands of FM-2.0-120. The average granular temperature remains relatively low before reaching the peak stress state, which indicates that at this stage the assembly deformation is relatively uniform at the particle scale, and the complex mesoscale structures have not yet formed. The granular temperature inside the shear

bands increases sharply at the start of strain softening, and the granular temperature outside the shear bands stays comparatively low. The many particle contacts and formation of circulation cells inside the shear bands result in higher granular temperatures compared to outside the shear bands. The fluctuation of granular temperature, especially inside the shear bands, also implies continuous slip–stick and stick–slip transitions in the granular material.

### 3.2 Spatial association of strain field and particle kinematics

In order to tackle the difficulty of calculating strain inside a particle assembly experiencing a localization pattern, a mesh-free method is employed in this work. The mesh-free strain calculation method was initially proposed by O’Sullivan et al. [47] and later improved by Wang et al. [61] and was recently employed by Zhu et al. [67] in their shear banding research. The method calculates the deformation gradient based on the particles’ translation and rotation, leading to an accurate and smooth strain field. Again, we make a comparison between the shear strain

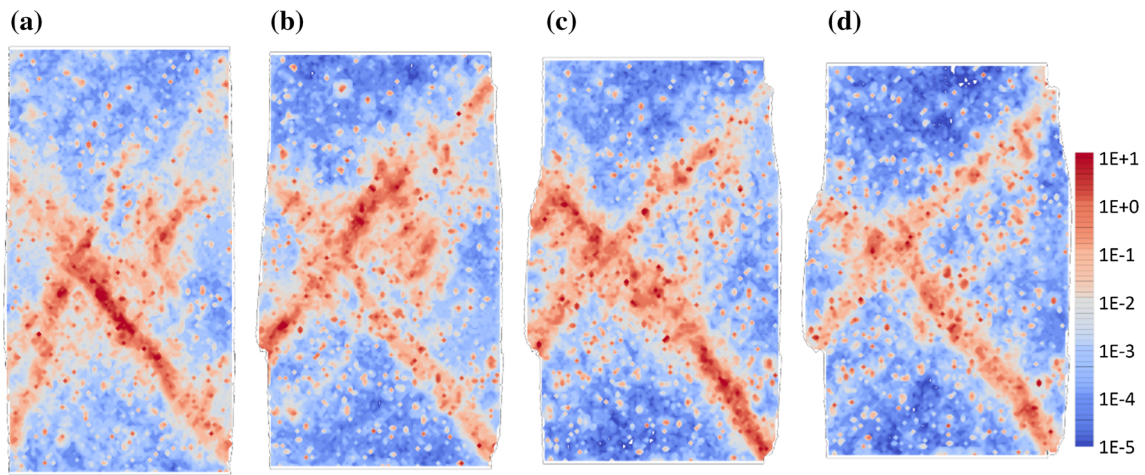


Fig. 11 Contours of granular temperature at different axial strain levels of FM-2.0-120: **a**  $\epsilon_a = 2.5\%$ ; **b**  $\epsilon_a = 5.0\%$ ; **c**  $\epsilon_a = 7.5\%$ ; **d**  $\epsilon_a = 10\%$

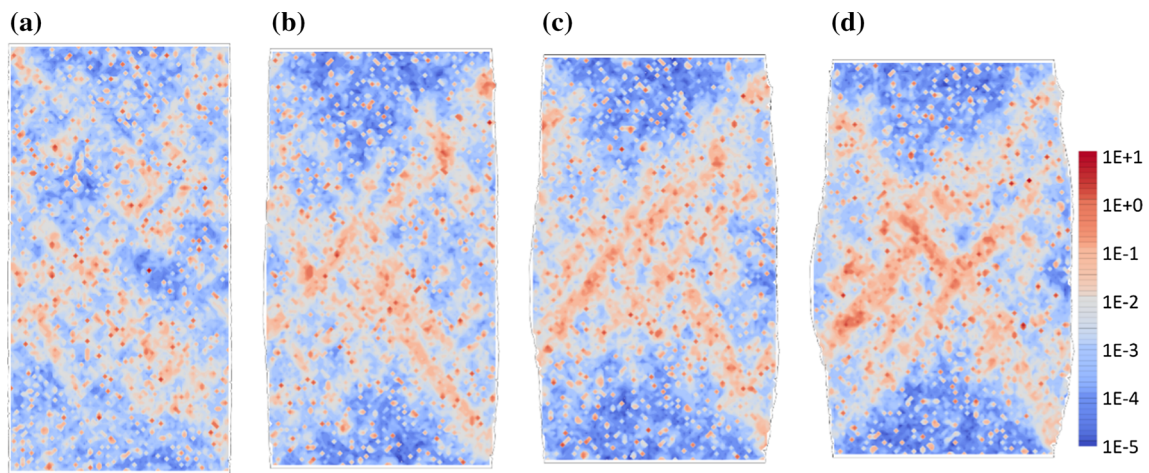


Fig. 12 Contours of granular temperature at different axial strain levels of FM-2.0-30: **a**  $\epsilon_a = 2.5\%$ ; **b**  $\epsilon_a = 5.0\%$ ; **c**  $\epsilon_a = 7.5\%$ ; **d**  $\epsilon_a = 10\%$

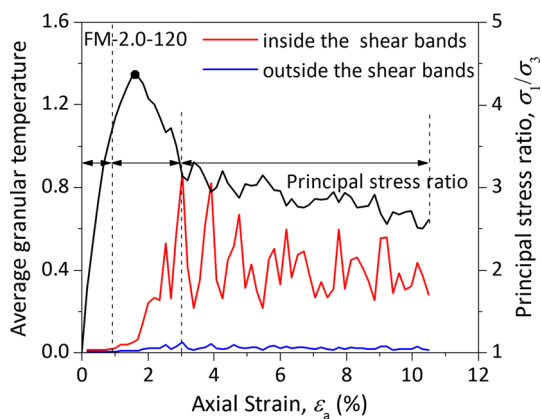


Fig. 13 Evolution of averaged granular temperature inside and outside shear bands of FM-2.0-120

field and particle kinematics of FM-2.0-120 on the square area depicted in Fig. 6a. When strain localization occurs, shear deformation mainly develops inside the shear bands,

whereas the adjacent material acts in a quasi-elastic manner. Therefore, due to structuring of the material, the material as a whole may no longer be described as a mechanical state of the material [67]. As the mesh-free method involves the two most important mechanisms in the calculation of strain field, i.e., particle rotation and a high level of non-affine deformation inside and outside the shear bands, it is not surprising that the shear strain field and kinematic quantities demonstrate strong degree of spatial association (as shown in Fig. 14).

## 4 Identification of shear bands

### 4.1 Variation of shear band thickness

Depending on the boundary conditions, loading rates, initial state of the material (mean effective stress and void ratio), gradation characteristics (grain size, uniformity,



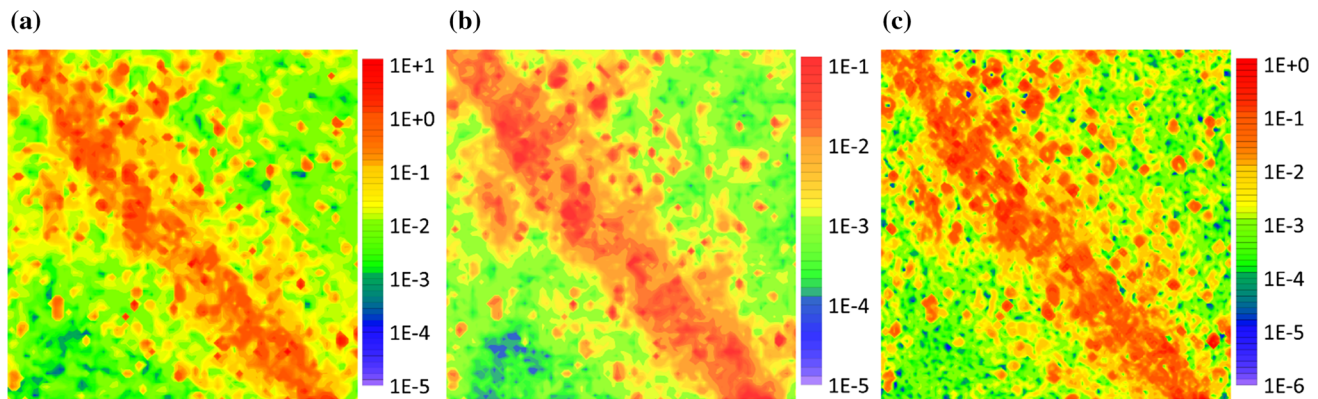


**Fig. 14** Strain field and particle kinematics in the square zone depicted in Fig. 6a: **a** shear strain field; **b** angular velocity; **c** relative velocity

etc.), and the size and slenderness of the specimen, shear bands of various widths can develop in a soil specimen [10]. For example, the shear band thickness tends to decrease with increasing particle size [4, 10], particle rolling coefficient [40], and confining pressure [13]. Few studies have shown that the band thickness decreases with decrease in initial void ratio or increase in density [13, 67]. However, Alshibli and Sture found that an increase in density would result in an increase in shear band thickness [4]. This study does not aim to delineate their disparities, but rather focus on the influence of particle crushability on shear band thickness.

We analyze the same region as shown in Fig. 6a to characterize the shear band in FM-2.0-120. Five profiles perpendicular to the shear band area framed by two solid black lines (Fig. 15a) are used to investigate the distributions of particle rotation, angular velocity, and granular temperature across the shear bandwidth. As shown in Fig. 15b–f, the value of these quantities is larger within the band and decreases rapidly when further away from the middle line of the shear band area. By superimposing the data points from the five profiles (Fig. 16), we can see clearly that the distributions of these quantities along the axis perpendicular to the middle line of shear band zone display prominent unimodal feature, i.e., they increase dramatically when approaching the center and oscillate near zero on both sides. Their distributions are fitted by a unimodal Gaussian function  $y = a \exp(-(x/b)^2)$ , where  $a$  and  $b$  are fitting parameters. As shown in Fig. 16, the points with small particle rotation, low angular velocity, and low fluctuating velocity are not accounted for in the curve fitting. The boundaries of shear band area can be approximated at the location where these quantities start to increase noticeably. The shear band thickness in FM-2.0-120 is estimated as  $2\delta \approx 0.2$ , which is approximately 8 times the mean particle diameter  $d_{50}$  prior to particle crushing.

Published experiments and DEM simulations show that shear band thicknesses are typically reported to be 8–20 times the mean particle diameter, and suggest a relationship of shear band thickness  $t_{\text{band}} \approx 10d_{50}$  for most cases [3, 14, 52, 53]. In our simulations, the shear band thickness normalized by  $d_{50}$  is 8 which is a little smaller than that usually found for sands and other granular materials. It may be attributed to two reasons: (1) the narrow particle size distribution and (2) high confining pressure. The shear band of a two-dimensional granular material composed of circular grains with a narrow range of particle diameters involves fewer particle sizes, e.g., 2–8 particle sizes [7, 18]. The high confining pressure would also confine the particle movement and thereby impede further propagation of shear banding. As demonstrated in Fig. 17, the shear band bounded by the solid lines increases in thickness with increase in particle crushability. The spread of the particle kinematics shown in Fig. 17 also implies that multiple localized events occur in highly crushable assembly. Therefore, it should be mentioned that the localization mechanism is more scattered and less intense than for low crushable assembly. As discussed in the previous section, the deformation pattern and failure mode in highly crushable assembly FM-2.0-30 are quite different from the localized mode observed in the other three assemblies. The failure mode of the highly crushable assembly can be regarded as a diffuse one, which is characterized by homogeneous deformation patterns without any apparent and persistent strain localization [67].

## 4.2 Onset of shear banding

It has been found that onset of shear banding is a pre-peak phenomenon, i.e., initiating during strain hardening [10, 64]. Tordesillas et al. [58] also noted in their experiments that the formation and location of the shear band may be decided in the earlier stages of loading, well before



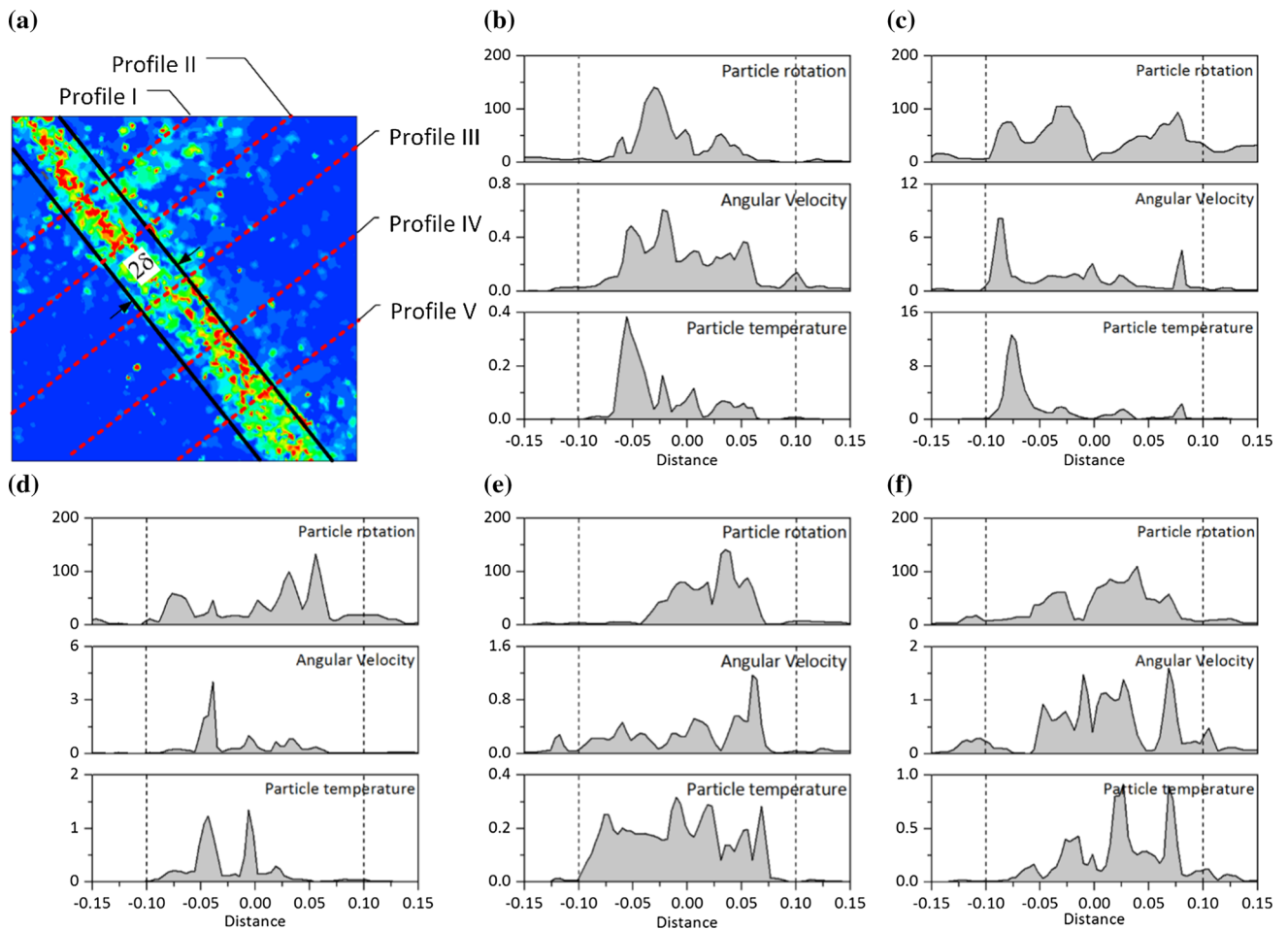


**Fig. 15** a Identification of shear band area in FM-2.0-120, framed between two solid black lines. The shear band thickness is denoted as  $2\delta$ ; **b–f** distributions of particle rotation, angular velocity, and granular temperature along the Profiles I to V perpendicular to shear band area (as demonstrated in a)

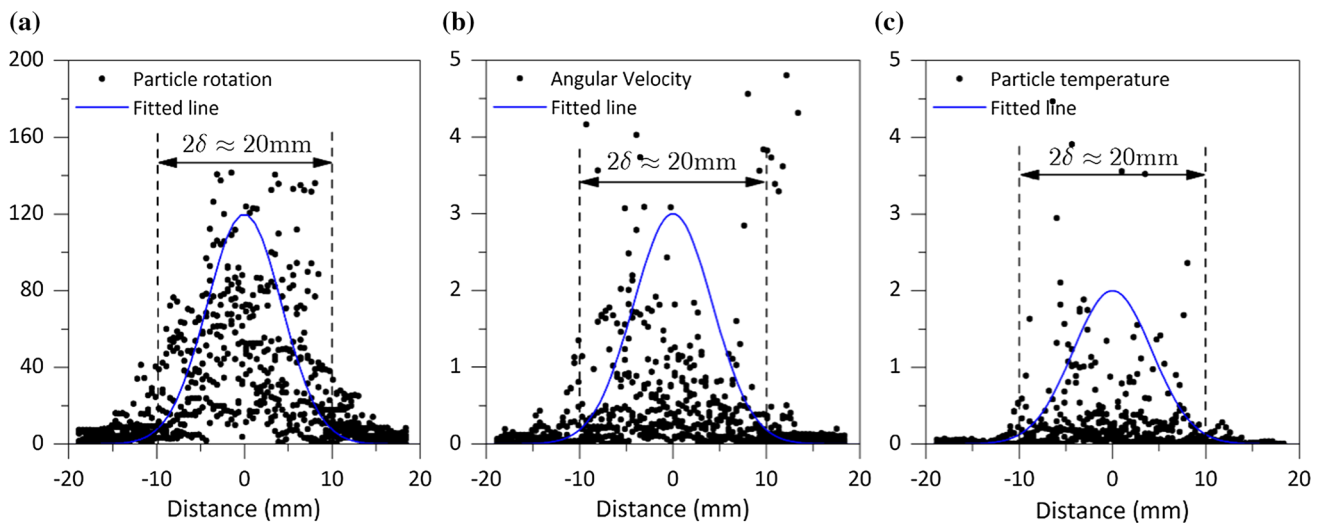


**Fig. 16** Superimposed plots of **a** particle rotation, **b** angular velocity and **c** granular temperature along the axis perpendicular to the middle line of shear band area. Scattered points are fitted by the solid line. Vertical dashed lines represent boundaries of the shear band area

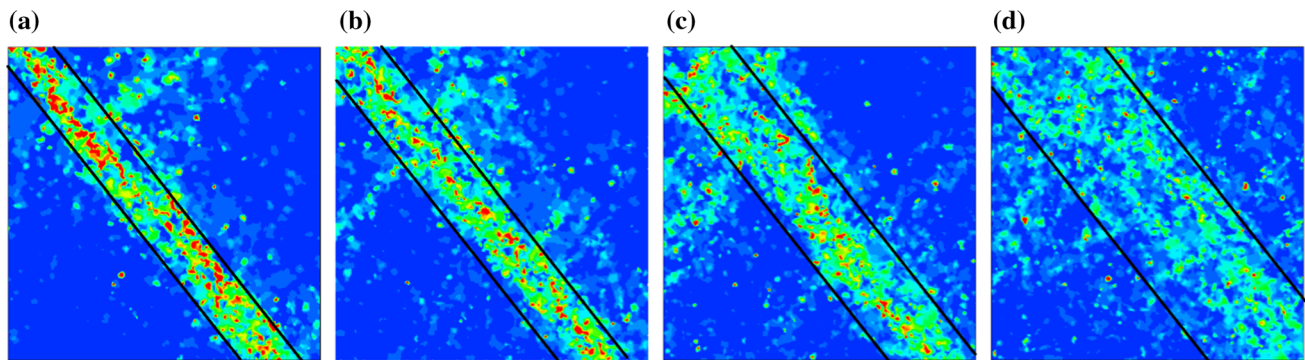


**Fig. 17** Failure pattern colored by magnitude of particle rotation for different levels of particle crushability: **a** FM-2.0-120; **b** FM-2.0-90; **c** FM-2.0-60; **d** FM-2.0-30

the peak stress. They found that the onset of shear banding coincides with the beginning of force chains buckling [58]. A general algorithmic identification of the occurrence of shear bands is difficult, especially regarding the identification of non-persistent shear bands of a loose sample, or a highly crushable sample. By conducting a statistical analysis of the kinematical quantities, e.g., particle angular velocity, fluctuating velocity, and granular temperature, we are able to reveal the main aspects of the strain localization process. Figure 18 presents histograms of granular temperature for FM-2.0-120. At the beginning of shearing, up to approximately 1% axial strain, in the granular temperature histogram of FM-2.0-120, a small number of particles begin to increase their “temperature”. This is because prior to onset of shear banding, intense shearing occurs within an evolving network of microbands. They have a smaller width and span over the entire assembly. These predominant deformation structures result in a slight increase in both the non-affine deformation and energy dissipation and therefore produce higher granular temperature [56].

Within the strain range at peak stress, another type of mesoscale structure with larger and stronger configuration, i.e., a vortex, starts to form and dominate the local deformation patterns, which causes the particle-scale non-affine strain suddenly to intensify and become localized along the

shear bands. The induced system disturbance can lead to an increase in granular temperature. Consequently, in the granular temperature histogram (Fig. 18), the boundary between green and blue areas rises sharply. The histogram also becomes more structured, showing evidence of a non-homogeneous material. The process of shear banding can be illustrated by the evolution of granular temperature corresponding to 97.5th and 99th percentiles (i.e., granular temperature of 97.5 and 99% particles smaller than this value). Figure 19 indicates that strain localization begins to develop rapidly (i.e., granular temperature increases) when an assembly reaches the peak shear stress. This phenomenon is much clearer in the low crushable assembly FM-2.0-120 (see Fig. 19a), which is consistent with the observation that strain localization develops more rapidly in an assembly with a lower degree of particle crushability.

## 5 Long-range correlation of contact networks

In this section, we analyze the influence of particle crushability on the structural properties of a particle assembly. We investigate the spatial force distribution

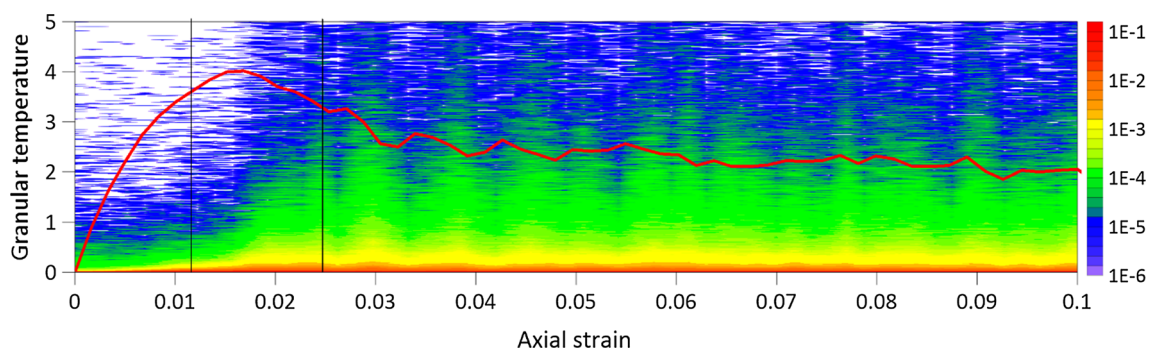


**Fig. 18** Granular temperature histogram map for FM-2.0-120 (The occurrences are encoded with color scale shown at right, and red line represents evolution of corresponding shear stress)

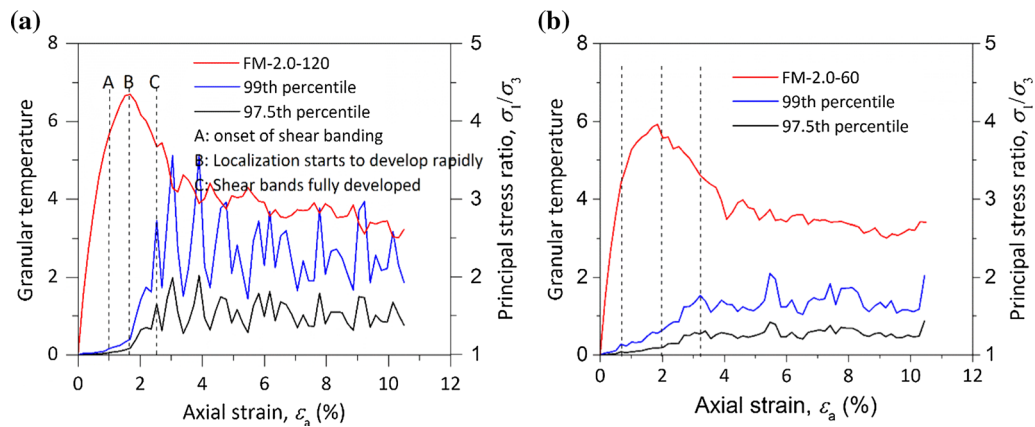


Fig. 19 Values of granular temperature corresponding to 97.5th and 99th percentiles for a FM-2.0-120 and b FM-2.0-60

through the calculation of a spatial force correlation function  $G(r)$  [27, 28, 54] as:

$$G(r) = \frac{\sum_{i=1}^N \sum_{j=i+1}^N \delta(|r_{ij} - r|) f_i f_j}{\sum_{i=1}^N \sum_{j=i+1}^N \delta(|r_{ij} - r|)} \quad (4)$$

where  $N$  is the total number of contact points,  $f_i$  is the normalized contact force at contact  $i$ ,  $r_{ij}$  is the distance between contacts  $i$  and  $j$ , and  $\delta(0) = 1$ . Therefore,  $G(r)$  measures the contribution of a pair of contact forces  $f_i$  and  $f_j$  separated by  $r_{ij}$  and summed over all contact points. A nonzero value of  $G(r)$  reveals that, on average, two contacts separated by a distance  $r$  have forces that are correlated.

The correlation indicates that two contacts at distance  $r$  are connected through a cluster of simultaneously contacting particles, and force from one particle is being transmitted through the network to the other particle [27]. It thereby gives a quantitative measurement of the average effect of force chains of length  $r$  in the assembly. Because the contact network is changing during shearing, the correlation function provides information on the average size of structures that are fluctuating in both space and time. Figure 20 plots the correlations of normal contact force for different crushable assemblies at the end of shearing. Note that the radial distance has been normalized by the mean particle diameter  $d_{50}$ . It shows that all assemblies have a strong peak near  $r = 0.3 \sim 0.4d_{50}$ , indicating that a correlation exists for a radial distance extending to less than one particle diameter. The peak decreases as particle crushability increases, suggesting weak packing due to intense particle crushing. We also note that the peaks shift to larger radial distances with increasing particle crushability. This behavior is consistent with less particle interlocking of increasingly crushable particles. Small oscillations around unity are observed when extending to greater than two mean particle diameters. The amplitude of oscillation is seen to decrease with increasing particle crushability and

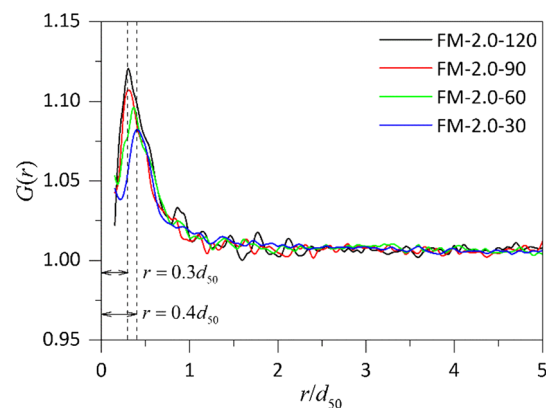
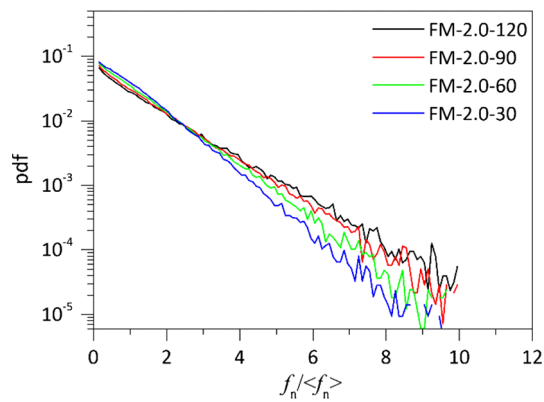


Fig. 20 Spatial force correlation function  $G(r)$  plotted as a function of distance  $r$  normalized by mean particle diameter  $d_{50}$  for different crushable assemblies at end of shearing

larger values of radial distance. In all, our results indicate that the contact forces are correlated, but only over short distances. With the increase in particle crushability, such correlation becomes weaker, indicating a more diffuse nature of force transmission across particle contacts.

The influence of particle crushability on the contact network can also be illustrated using the probability distribution function (PDF) of contact forces. The normal contact forces of different assemblies are normalized by their corresponding mean normal force. As shown in Fig. 21, all PDFs are nearly linearly distributed in log-linear scales. The highly crushable assembly is characterized by a larger proportion of weak forces ( $f_n < \langle f_n \rangle$ ) and a smaller number of strong forces, and the low crushable assembly is the opposite. The downward trend of PDFs with increasing particle crushability implies that the inhomogeneity of normal forces becomes lower as the particles become more crushable. In other words, that the proportion of strong contacts declines with increasing particle crushability is a clear sign of weakened force chain networks.



**Fig. 21** Probability distribution function of normal contact forces  $f_n$  normalized by mean normal force  $\langle f_n \rangle$  in log-linear scales for different assemblies at end of shearing

## 6 Discussion

Based on a 2D plane strain FDEM simulation, which may not fully represent the real soil behavior, the observations made of the relationship between onset and subsequent development of strain localization and particle crushability in this paper have provided a basis for the development of micromechanics-based constitutive models for crushable soils in future studies. Therefore, it is time to have a second look, with the particle kinematical information, to assess what can be added to a current constitutive modeling framework. At present, it is still unclear how to rationally introduce microscopic behavior of granular geomaterials into a well-established constitutive framework. Some researchers have attempted to develop micromechanics-based constitutive models for shear band modeling in granular materials, in which the macroscopic parameters are derived with respect to the particle-scale structure and information [42, 49, 63]. However, most of the micromechanics-based constitutive models have not been fully accepted, mainly because they are not as straightforward as conventional phenomenological models. Besides, the aforementioned studies have not considered the role of particle crushing in strain localization and shear banding behavior. Some pioneering works have attempted to develop a rational and rigorous constitutive model for granular materials accounting for particle crushing associated with micromechanics [44]. Building upon the micromechanics-based approaches mentioned above, it is possible that our work could provide a changeable internal length scale that is used to describe the shear band thickness in a micropolar constitutive theory [60].

Another way of incorporating our findings into constitutive modeling of granular materials is based on a hierarchical multiscale framework. With the coupling of FEM and DEM, hierarchical multiscale modeling of granular

materials has been proposed by several researchers [15, 16, 26, 39, 45]. The FEM is employed to discretize the continuum domain of a boundary value problem (BVP) into FE mesh and to solve the governing equations over the discretized domain. To date, such research has only considered uncrushable particle assemblies at each Gauss point of the FEM mesh, which receives boundary conditions from the FEM and is solved by DEM to derive the local constitutive response. As highlighted in this paper, particle crushing has a significant effect on shear banding behavior. Thus, there will be a need to add the crushable particle feature in future FEM/DEM hierarchical multiscale modeling efforts.

## 7 Conclusions

The cohesive crack model is introduced into the combined finite discrete element method (FDEM) to simulate particle crushing on the basis of damage mechanics. This development makes combined FDEM an ideal tool for modeling irregularly shaped and crushable granular materials. An exploration has been conducted on the influence of particle crushability on particle kinematics and shear banding of granular materials. Lateral flexible boundary conditions are employed to mimic realistic laboratory biaxial tests, although all FDEM simulations are 2D plane strain. Due to distortion of specimens, the “real” stress tensor is calculated by defining a kinematically moving mask inside the specimen. The main conclusions of the study are summarized as follows:

1. For the highly crushable assembly, many irregular and local zones of strain localization are observed, but they fail to form a connected zone, and therefore, no distinct shear band is formed. The distributions of particle kinematical quantities indicate that the mesoscale structures, like microbands and vortices, are much weaker due to the erratic contact between neighboring particles of increasing crushability. The sparsity of large fluctuating velocity in highly crushable assemblies also indicates a fragmented deformation pattern due to intense particle crushing.
2. The mesh-free strain calculation method includes the two most important mechanisms in the calculation of strain, i.e., particle translation and rotation. High degrees of spatial associations occur amongst the shear strain, angular velocity, and fluctuating velocity, which confirms the key role that non-affine deformation and particle rotation play in shear band formation. It also verifies the usage of particle kinematics to identify shear bandwidth and the onset and subsequent development of shear banding. Our results indicate that



shear bandwidth increases, and the development speed slows down, with increasing particle crushability.

- The spatial force correlation functions for different crushable assemblies demonstrate that the contact forces are correlated, but only over short distances. With the increase in particle crushability, such correlation becomes weaker, indicating a more diffuse nature of force transmission across particle contacts for weaker particles. The probability distribution functions of normal contact force suggest that the inhomogeneity of normal forces becomes lower as the particles become more crushable. All evidence suggests a weakening of particle crushing influence on the contact network.

**Acknowledgements** This work was financially supported by the National Key Research and Development Program of China (No. 2017YFC0404801), National Natural Science Foundation of China (No. 51509190), and China Postdoctoral Science Foundation (No. 2016T907272). We also thank the anonymous reviewers for their constructive reviews.

## References

- Ai J, Langston PA, Yu HS (2014) Discrete element modelling of material non-coaxiality in simple shear flows. *Int J Numer Anal Methods Geomech* 38(6):615–635
- Alikarami R, Andò E, Gkiousas-Kapnisis M et al (2015) Strain localisation and grain breakage in sand under shearing at high mean stress: insights from in situ X-ray tomography. *Acta Geotechnica* 10(1):15–30
- Alshibli KA, Hasan A (2008) Spatial variation of void ratio and shear band thickness in sand using X-ray computed tomography. *Geotechnique* 58(4):249–257
- Alshibli KA, Sture S (1999) Sand shear band thickness measurements by digital imaging techniques. *J Comput Civ Eng* 13(2):103–109
- Alshibli KA, Sture S (2000) Shear band formation in plane strain experiments of sand. *J Geotech Geoenviron Eng* 126(6):495–503
- Ando E, Hall SA, Viggiani G et al (2012) Grain-scale experimental investigation of localised deformation in sand: a discrete particle tracking approach. *Acta Geotechnica* 7(1):1–13
- Calvetti F, Combe G, Lanier J (1997) Experimental micromechanical analysis of a 2D granular material: relation between structure evolution and loading path. *Mechan Cohesive Frict Mater* 2(2):121–163
- Campbell CS (2006) Granular material flows—an overview. *Powder Technol* 162(3):208–229
- Cheung G, O’Sullivan C (2008) Effective simulation of flexible lateral boundaries in two- and three-dimensional DEM simulations. *Particuology* 6(6):483–500
- Desrues J, Viggiani G (2004) Strain localization in sand: an overview of the experimental results obtained in Grenoble using stereophotogrammetry. *Int J Numer Anal Meth Geomech* 28(4):279–321
- Druckrey AM, Alshibli KA, Al-Raoush RI (2016) 3D characterization of sand particle-to-particle contact and morphology. *Comput Geotech* 74:26–35
- Fu P, Dafalias YF (2011) Fabric evolution within shear bands of granular materials and its relation to critical state theory. *Int J Numer Anal Methods Geomech* 35(18):1918–1948
- Gu X, Huang M, Qian J (2014) Discrete element modeling of shear band in granular materials. *Theoret Appl Fract Mech* 72:37–49
- Guo P (2012) Critical length of force chains and shear band thickness in dense granular materials. *Acta Geotechnica* 7(1):41–55
- Guo N, Zhao J (2014) A coupled FEM/DEM approach for hierarchical multiscale modelling of granular media. *Int J Numer Methods Eng* 99(11):789–818
- Guo N, Zhao J (2016) 3D multiscale modeling of strain localization in granular media. *Comput Geotech* 80:360–372
- Hall SA, Bornert M, Desrues J et al (2010) Discrete and continuum experimental study of localised deformation in Hostun sand under triaxial compression using X-ray  $\mu$ CT and 3D digital image correlation. *Géotechnique* 60(5):315–322
- Hall SA, Wood DM, Ibraim E et al (2010) Localised deformation patterning in 2D granular materials revealed by digital image correlation. *Granul Matter* 12(1):1–14
- Hasan A, Alshibli KA (2010) Experimental assessment of 3D particle-to-particle interaction within sheared sand using synchrotron microtomography. *Géotechnique* 60(5):369
- Hurley RC, Hall SA, Andrade JE et al (2016) Quantifying interparticle forces and heterogeneity in 3D granular materials. *Phys Rev Lett* 117(9):098005
- Iwashita K, Oda M (2000) Micro-deformation mechanism of shear banding process based on modified distinct element method. *Powder Technol* 109(1):192–205
- Jiang MJ, Yu HS, Harris D (2005) A novel discrete model for granular material incorporating rolling resistance. *Comput Geotech* 32(5):340–357
- Karatza Z, Andò E, Papanicolopulos SA et al (2017) Evolution of deformation and breakage in sand studied using X-ray tomography. *Géotechnique* 1:1–11
- Kuhn MR (1999) Structured deformation in granular materials. *Mech Mater* 31(6):407–429
- Kuhn MR, Bagi K (2004) Contact rolling and deformation in granular media. *Int J Solids Struct* 41(21):5793–5820
- Liu Y, Sun WC, Yuan Z et al (2015) A nonlocal multiscale discrete-continuum model for predicting mechanical behavior of granular materials. *Int J Numer Methods Eng* 106:129–160
- Lois G, Lemaître A, Carlson JM (2007) Spatial force correlations in granular shear flow. II. Theoretical implications. *Phys Rev E* 76(2):021303
- Løvoll G, Måløy KJ, Flekkøy EG (1999) Force measurements on static granular materials. *Phys Rev E* 60(5):5872
- Ma G, Zhou W, Chang XL et al (2013) Combined FEM/DEM modeling of triaxial compression tests for rockfills with polyhedral particles. *Int J Geomech* 14(4):04014014
- Ma G, Chang XL, Zhou W et al (2014) Mechanical response of rockfills in a simulated true triaxial test: a combined FDEM study. *Geomech Eng* 7(3):317–333
- Ma G, Zhou W, Chang XL (2014) Modeling the particle breakage of rockfill materials with the cohesive crack model. *Comput Geotech* 61(9):132–143
- Ma G, Zhou W, Ng TT et al (2015) Microscopic modeling of the creep behavior of rockfills with a delayed particle breakage model. *Acta Geotechnica* 10(4):481–496
- Ma G, Zhou W, Chang X et al (2016) Formation of shear bands in crushable and irregularly shaped granular materials and the associated microstructural evolution. *Powder Technol* 301:118–130
- Ma G, Zhou W, Chang XL et al (2016) A hybrid approach for modeling of breakable granular materials using combined finite-discrete element method. *Granul Matter* 18(1):1–17

35. Ma G, Zhou W, Regueiro RA et al (2017) Modeling the fragmentation of rock grains using computed tomography and combined FDEM. *Powder Technol* 308:388–397
36. Mahmood Z, Iwashita K (2010) Influence of inherent anisotropy on mechanical behavior of granular materials based on DEM simulations. *Int J Numer Anal Methods Geomech* 34(8):795–819
37. Mahmood Z, Iwashita K (2011) A simulation study of microstructure evolution inside the shear band in biaxial compression test. *Int J Numer Anal Methods Geomech* 35(6):652–667
38. Majmudar TS, Behringer RP (2005) Contact force measurements and stress-induced anisotropy in granular materials. *Nature* 435(7045):1079–1082
39. Miede C, Dettmar J, Zäh D (2010) Homogenization and two-scale simulations of granular materials for different microstructural constraints. *Int J Numer Methods Eng* 83(8–9):1206–1236
40. Mohamed A, Gutierrez M (2010) Comprehensive study of the effects of rolling resistance on the stress–strain and strain localization behavior of granular materials. *Granul Matter* 12(5):527–541
41. Munjiza AA, Knight EE, Rougier E (2011) *Computational mechanics of discontinua*. Wiley, New York
42. Nemat-Nasser S (2000) A micromechanically-based constitutive model for frictional deformation of granular materials. *J Mech Phys Solids* 48(6):1541–1563
43. Nemat-Nasser S, Okada N (2001) Radiographic and microscopic observation of shear bands in granular materials. *Geotechnique* 51(9):753–766
44. Nguyen GD, Einav I (2010) Nonlocal regularisation of a model based on breakage mechanics for granular materials. *Int J Solids Struct* 47(10):1350–1360
45. Nguyen T, Combe G, Caillerie D et al (2014) FEM × DEM modelling of cohesive granular materials: numerical homogenisation and multi-scale simulations. *Acta Geophys* 62(5):1109–1126
46. Oda M, Takemura T, Takahashi M (2004) Microstructure in shear band observed by microfocus X-ray computed tomography. *Geotechnique* 54(8):539–542
47. O’Sullivan C, Bray JD, Li S (2003) A New approach for calculating strain for particulate media. *Int J Numer Anal Methods Geomech* 27(10):859–877
48. Potyondy DO, Cundall PA (2004) A bonded-particle model for rock. *Int J Rock Mech Min Sci* 41(8):1329–1364
49. Qian J, You Z, Huang M et al (2013) A micromechanics-based model for estimating localized failure with effects of fabric anisotropy. *Comput Geotech* 50:90–100
50. Radjai F, Roux S (2002) Turbulentlike fluctuations in quasistatic flow of granular media. *Phys Rev Lett* 89(6):064302
51. Rechenmacher AL (2006) Grain-scale processes governing shear band initiation and evolution in sands. *J Mech Phys Solids* 54(1):22–45
52. Sadrekarimi A, Olson SM (2009) Shear band formation observed in ring shear tests on sandy soils. *J Geotech Geoenviron Eng* 136(2):366–375
53. Sibille L, Hadda N, Nicot F et al (2015) Granular plasticity, a contribution from discrete mechanics. *J Mech Phys Solids* 75:119–139
54. Silbert LE, Grest GS, Landry JW (2002) Statistics of the contact network in frictional and frictionless granular packings. *Phys Rev E* 66(6):061303
55. Tatone BSA, Grasselli G (2015) A calibration procedure for two-dimensional laboratory-scale hybrid finite–discrete element simulations. *Int J Rock Mech Min Sci* 75:56–72
56. Tordesillas A, Muthuswamy M, Walsh SD (2008) Mesoscale measures of nonaffine deformation in dense granular assemblies. *J Eng Mech* 134(12):1095–1113
57. Tordesillas A, Lin Q, Zhang J et al (2011) Structural stability and jamming of self-organized cluster conformations in dense granular materials. *J Mech Phys Solids* 59(2):265–296
58. Tordesillas A, Walker DM, Andò E et al (2013) Revisiting localized deformation in sand with complex systems. *Proc R Soc A R Soc* 469(2152):20120606
59. Utter B, Behringer RP (2004) Self-diffusion in dense granular shear flows. *Phys Rev E* 69(3):031308
60. Voyiadjis GZ, Alsaleh MI, Alshibli KA (2005) Evolving internal length scales in plastic strain localization for granular materials. *Int J Plast* 21(10):2000–2024
61. Wang J, Dove JE, Gutierrez MS (2007) Discrete-continuum analysis of shear banding in the direct shear test. *Géotechnique* 57(6):513–526
62. Williams JR, Rege N (1997) The development of circulation cell structures in granular materials undergoing compression. *Powder Technol* 90(3):187–194
63. Yang Y, Misra A (2012) Micromechanics based second gradient continuum theory for shear band modeling in cohesive granular materials following damage elasticity. *Int J Solids Struct* 49(18):2500–2514
64. Zhou B, Huang R, Wang H et al (2013) DEM investigation of particle anti-rotation effects on the micromechanical response of granular materials. *Granul Matter* 15(3):315–326
65. Zhou W, Ma G, Chang X et al (2013) Influence of particle shape on behavior of rockfill using a three-dimensional deformable DEM. *J Eng Mech* 139(12):1868–1873
66. Zhou W, Yang L, Ma G et al (2017) DEM modeling of shear bands in crushable and irregularly shaped granular materials. *Granul Matter* 19(2):25
67. Zhu H, Nguyen HNG, Nicot F et al (2016) On a common critical state in localized and diffuse failure modes. *J Mech Phys Solids* 95:112–131